PCCP

ROYAL SOCIETY OF CHEMISTRY

PAPER

View Article Online
View Journal | View Issue

Check for updates

Cite this: *Phys. Chem. Chem. Phys.*, 2025, **27**, 6687

Theoretical evaluation of Na_2MgCl_4 double chlorite as an electrolyte for all-solid-state sodium-ion batteries†

Yohandys A. Zulueta, [a] Jose R. Fernández-Gamboa, [a] Narciso Antonio Villar Goris, [b] My Phuong Pham-Ho [cd] and Minh Tho Nguyen *[ef]

The quest for effective and exceptional solid-state electrolytes for metal ion batteries has to address two primary challenges: overcoming the interfacial resistance between the solid-state electrolyte and the electrodes and improving their relatively low dc conductivity at operating temperatures. This study presents advanced atomistic simulations of the primary properties of the Na_2MgCl_4 double chlorite compound. Calculated results revealed that Na_2MgCl_4 possessed key properties suitable for a solid-state electrolyte in energy storage applications. Influenced by the hybridizations of $[MgCl_6]$ and $[NaCl_6]$, Na_2MgCl_4 exhibited insulator properties with an energy band gap of 4.7 eV. Mechanical properties suggested that Na_2MgCl_4 was a stable and ductile compound with favorable bulk, shear, and Young's moduli, thereby ensuring compatibility and stability with potential electrodes. Defect energetics highlighted the NaCl Schottky defects as the most abundant, with Zn^{2+} and Ga^{3+} as effective dopants that enhanced Na-vacancy concentration, impacting large-scale transport properties. From the evaluation using the bond valence site energy method, Na_2MgCl_4 possesses excellent Na activation energies for diffusion (0.20 eV) and conduction (0.17 eV) along with high diffusivity of 0.17 mS cm^{-1} and conductivity of 1.65×10^{-9} cm^2 s^{-1} at 300 K. These attributes were competitive with those of the current solid-state electrolytes, underscoring the potential of Na_2MgCl_4 for high-performance battery applications. Overall, Na_2MgCl_4 meets the essential criteria to be used as a solid-state electrolyte in Na-ion batteries.

Received 19th January 2025,
Accepted 27th February 2025

DOI: 10.1039/d5cp00254k

rsc.li/pccp

Open Access Article. Published on 28 February 2025. Downloaded on 2/21/2026 7:17:04 PM.
This article is licensed under a Creative Commons Attribution-NonCommercial 3.0 Unported Licence.

1. Introduction

Global efforts towards decarbonization have positioned battery materials as pivotal elements in the advancement of electrification of transportation and storage of intermittent solar and wind energy.[1–4] Lithium-ion batteries have become ubiquitous, driving a revolution in portable electronics and the automotive industry. However, the widespread adoption of electrochemical energy storage for large-scale applications, such as electromobility and grid storage, requires batteries to meet some stringent criteria in terms of their performance, safety, energy density, and more importantly the final cost.[1–10] Current state-of-the-art battery technologies still fall short of fulfilling these requirements.

In the present context of rapidly developing battery industry, research efforts are primarily focused on two approaches: the first involves incremental improvements in the well-established Li-ion technology, and the second approach focuses on significant modifications to its core components (post-Li-ion battery). The latter approach motivates extensive investigations into alternative mobile cations such as the Na-ion, the use of metallic anodes, and the development of solid electrolytes to create solid-state batteries. These post-Li-ion strategies can be combined to tailor battery characteristics to specific application requirements.[10–12]

The intercalation chemistry of Li and Na metal ions is quite similar, making the materials tested for Li-ion batteries (LIB) potentially applicable to Na-ion systems (NIB) and *vice versa*. Both systems operate on the same basic principles, and therefore,

[a] *Departamento de Física, Facultad de Ciencias Naturales y Exactas, Universidad de Oriente, Santiago de Cuba, CP 90500, Cuba*
[b] *Autonomous University of Santo Domingo (UASD), Dominican Republic*
[c] *Faculty of Chemical Engineering, Ho Chi Minh City University of Technology (HCMUT), 268 Ly Thuong Kiet Str., District 10, Ho Chi Minh City, 70000, Vietnam*
[d] *Vietnam National University Ho Chi Minh City, Linh Trung, Thu Duc, Ho Chi Minh City, 70000, Vietnam*
[e] *Laboratory for Chemical Computation and Modeling, Institute for Computational Science and Artificial Intelligence, Van Lang University, Ho Chi Minh City, 70000, Vietnam. E-mail: minhtho.nguyen@vlu.edu.vn*
[f] *Faculty of Applied Technology, School of Technology, Van Lang University, Ho Chi Minh City, 70000, Vietnam*

† Electronic supplementary information (ESI) available. See DOI: https://doi.org/10.1039/d5cp00254k

Open Access Article. Published on 28 February 2025. Downloaded on 2/21/2026 7:17:04 PM.
This article is licensed under a Creative Commons Attribution-NonCommercial 3.0 Unported Licence.

the existing Li-ion battery (LIB) manufacturing infrastructure can be adapted to produce NIBs, representing a significant advantage for the investment and support of this technology.[12–14] Despite this fact, sodium-ion batteries exhibiting high energy densities are currently limited, and it is challenging to improve the NIBs using existing liquid electrolyte systems.[12–14] A viable strategy involves the replacement of the liquid electrolyte with a solid electrolyte, which also acts as a physical barrier to dendrite growth. However, practical applications of all-solid-state Na batteries are still constrained by the deficiencies of solid electrolytes, such as low ionic conductivity at room temperature, narrow electrochemical window, and weak chemical/electrochemical stability.[15–17]

Along with experimental investigations, computations are playing a crucial role in discovering new solid-state electrolytes (SSEs) for sodium-ion batteries.[18–25] These computational methods provide us with valuable insights into the fundamental mechanisms of SSEs, thus accelerating their development. Computational techniques such as atomistic first-principles calculations, molecular dynamics simulations, bond-valence site energy (BVSE) and force field methods (FF) are extensively employed to investigate the properties of solid-state electrolyte (SSE) compounds.[18–23] Insights from advanced atomistic simulations, among others, can guide the design of SSEs with high ion diffusivity, chemical stability, and broad electrochemical stability windows, and then ultimately advance all-solid-state battery technology.[17–25]

Halide solid electrolytes offer excellent chemical stability, crucial for maintaining battery performance over numerous charge–discharge cycles. Their durability helps prevent degradation and ensures long-term reliability. Moreover, their scalability makes them a viable option for large-scale battery manufacturing, which is beneficial for commercial applications. These factors drive the ongoing research in this area.[24–28]

Of sodium double chlorides, five structural types have been reported, including the olivine and the Sr_2PbO_4-type structures for a family of Na_2MCl_4 compounds with M being a metal element such as Co, Zn, Mg, Mn, Fe, and Cd. The ionic conductivities of these double chlorides with a Sr_2PbO_4-type structure were reported to be around 10^{-6} to 10^{-8} S cm^{-1} at 200 °C.[29,30] Previous studies aimed to design and optimize the geometric structure of Na_2MgCl_4 and critically examined the vibrational spectra and thermodynamic properties that are useful in chemical catalysis, ion battery manufacturing, and the design of novel functional materials.[31] However, the mechanical properties and ion conduction mechanisms of the Na_2MgCl_4 series remain unexplored. In this context, we set out to disclose in this study the capabilities of the double halide Na_2MgCl_4 as a battery material by using advanced atomistic simulations.

2. Methodology

Density functional theory (DFT) calculations are conducted using the CASTEP code to investigate the structural, electronic, and mechanical properties of the Na_2MgCl_4 structure.[32] The GGA-PBESOL exchange–correlation functional within the generalized gradient approximation is employed.[33] Ultrasoft pseudopotentials with a plane-wave energy cutoff of 830 eV are utilized. Specifically, the pseudoatomic functions for Na-$2s^2 2p^6 3s^1$, Mg-$2p^6 3s^2$, and Cl-$3s^2 3p^5$ in reciprocal space represent the electronic configurations of the constituent atoms.

For self-consistent computations and geometry optimizations, we set convergence thresholds as follows: a total energy change of 5×10^{-6} eV per atom, and maximum force, stress, and atomic displacements of 10^{-2} eV Å^{-1}, 2×10^{-2} GPa, and 5×10^{-4} Å, respectively. Additionally, a $4 \times 4 \times 4$ k-point mesh, following the Monkhorst–Pack method, is used to sample the Brillouin zone.[34]

The general utility lattice program (GULP) is used to explore the structural and mechanical properties of the compound considered, including defect energetics computations.[35] The potential parameters (force field values) are taken from previous studies.[18,27,36,37] The Buckingham model is used for the short-range interactions. Long-range interactions are treated as Coulombic interactions where only the charge and the interatomic distance describe the long-range potential energy. The Dick and Overhauser model is included for treatment of the ionic polarization,[38] which considers each ion as a positively charged core and a negatively charged shell, linked by a spring (with spring constant k), and the sum of the core–shell charges results in the formal charge (Z) of the polarizable ion.[38]

The multi-region strategy, which is also known as the Mott–Littleton method, is used for defect calculations.[39] In this approximation, the crystal structure is divided into two concentrically spherical regions with radii of $R1$ and $R2$ where $R1 < R2$. The isolated defect or defect cluster is located in the $R1$ sphere where the interaction between the defect/cluster and the local structure is strong. The region $R2$ is treated by a quasi-continuum approximation.[39,40] To obtain high accuracy for the defect energetics calculations, the value of $R1$ should be greater than the maximum short-range cut-off provided by the force field parameters and the difference between $R2$ and $R1$ must be close to (or higher than) the force field cut-off. Values of $R1$ = 13 Å and $R2$ = 27 Å are adopted, ensuring convergence of the computations. The Broyden–Fletcher–Goldfarb–Shanno algorithm is adopted to update the cell parameters and fractional positions during the defect energetic and geometry optimization computations.[35,40]

The common methodology used to study defect energetics is based on the Mott–Littleton method where the defect or defect cluster is simulated at the infinitely dilute limit.[35,40] The total defect energy, E_T, is described by eqn (1):

$$E_T = E_1(x) + E_{12}(x,\epsilon) + E_2(\epsilon) \quad (1)$$

where the interatomic displacements in the inner region are denoted by x and the external by ϵ, E_1 and E_2 represent the energies of $R1$ and $R2$, respectively, and E_{12} is the interchange energy between the regions. This technique has previously been used to explore the defect formation in solid-state battery materials.[18,19,25,37]

 This journal is © the Owner Societies 2025

Open Access Article. Published on 28 February 2025. Downloaded on 2/21/2026 7:17:04 PM.
This article is licensed under a Creative Commons Attribution-NonCommercial 3.0 Unported Licence.

The bond-valence site energy method turns out to be a simple and effective way of rapidly delivering diffusion paths and activation energies for both diffusion and conduction processes in solid state materials.[20,21,23] Briefly, this method identifies the regions of low bond valence site energy of a mobile cation. The bond length between a cation A and an anion, denoted as X (L_{A-X}), is evaluated using the tabulated empirical parameters $L_{0,A-X}$ and b_{A-X}. The individual bond valence (s_{A-X}) is then determined by eqn (2):

$$s_{A-X} = \exp[(L_{0,A-X} - L_{A-X})/b_{A-X}] \quad (2)$$

The bond valence site energy of a cation A [$E_{BVSE}(A)$] is evaluated similarly to Morse empirical potentials by adding the Coulombic repulsive term (E_r) of the mobile A ion with respect to other static ions, as expressed in eqn (3):[20,21,23]

$$E_{BVSE}(A) = \sum_X D_0 \left[\sum_{i=1}^{N} \left[\left(s_{A-X}/s_{\min,A-X} \right)^2 - 2 s_{A-X}/s_{\min,A-X} \right] \right] + E_r \quad (3)$$

The bond valence pathway analyser code (softBV-GUI) is used for the computation of the quantity E_{BVSE} and the required parameters in eqn (3) are included within the code.[41] In the study of $E_{BVSE}(Na^+)$, the Coulombic repulsion between mobile Na^+ and fixed M^{2+} cations is considered, while Coulombic attractive interactions are included in the Morse-type attraction terms. Migration paths for Na^+ ions follow regions of low bond valence site energy in mesh grids wrapping the Na_2MgCl_4 lattice structure with a resolution of ± 0.1 Å^3.[20,21,23,41]

3. Results and discussion

3.1 Structural and electronic properties of Na_2MgCl_4

An understanding of the fundamental properties such as structural, electronic and mechanical characteristics is crucial for determining any potential technological application of a material. For example, in hybrid automotive vehicles, the weight and size of the battery significantly influence energy consumption. Therefore, for new or less explored compounds, it is imperative to make predictions using appropriate computations to ensure accurate assessments. In this work, density functional theory (DFT) is employed for this purpose.

Fig. 1 displays the unit cell of the Na_2MgCl_4 lattice structure. Fig. 1a presents the view along the [001] direction, while Fig. 1b shows the view along the [$\bar{1}$00] direction, highlighting the arrangement of the $MgCl_6$] and [$NaCl_6$] polyhedral. The Na_2MgCl_4 compound crystallizes in an orthorhombic Pbam space group. Na^+ ions are coordinated by six Cl^- ions, whereas Mg^{2+} is bonded to six Cl^- ions, creating an edge-sharing [$MgCl_6$] octahedron.

The lattice parameters obtained from both DFT and force field computations are summarized in Table 1. The cell parameters derived from both methods are close to the available experimental values.[30] Additionally, the reduction in cell parameters obtained using the force field method is less than 5% as compared to those reported in the literature, indicating that the force field used in this work can accurately reproduce the lattice parameters of Na_2MgCl_4. On the other hand, as expected, DFT computations result in better reproducibility of the lattice parameters.

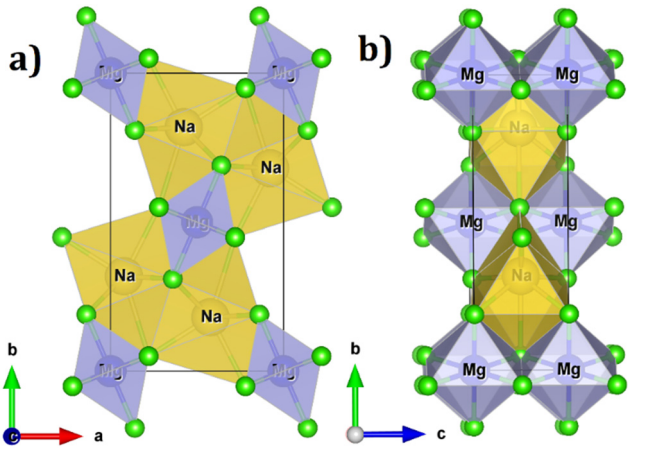

Fig. 1 Unit cell of Na_2MgCl_4 in the conventional representation (space group Pbam, No. 55): (a) and (b) views along the [001] and [$\bar{1}$00] directions, respectively. Blue and green spheres represent the Mg^+ and Cl^- ions, while blue and orange polyhedra represent the [$MgCl_6$] and [$NaCl_6$] octahedra, respectively.

Table 1 Results of lattice parameters of the optimized Na_2MgCl_4 (space group number 55) derived from different approaches

Lattice parameters (in Å)	Force field	DFT	Experimental ref. 30
a	6.853 (−0.8%)	6.916 (+0.1%)	6.907
b	11.342 (−4.6%)	11.873 (−0.1%)	11.885
c	3.710 (−2.7%)	3.817 (+0.1%)	3.814

The electronic properties of a material are essential for assessing its performance as a solid-state electrolyte (SSE). For battery materials, a good electronic and ionic conductivity are crucially required. Fig. 2a illustrates the band structure of Na_2MgCl_4, highlighting its insulating nature through an indirect band gap (Z to Γ point) of E_g = 4.7 eV near the valence band (with the Fermi level set at 0 eV). A large amount of electrons is present at the bottom of the conduction band at the Z point, which can easily be excited by an external electromagnetic field or thermal energy, facilitating their transition to the top of the conduction band at the Γ point and *vice versa*. To the best of our knowledge, no previous report is available on the energy gap of this compound.

The total density of states (DOS) and the projected density of states (PDOS) for Na_2MgCl_4 are depicted in Fig. 2b. The valence band is primarily dominated by Cl-states, while the conduction band is mainly influenced by Na-states. Minor contributions from Cl-p atomic orbitals to the conduction band are observed, and also from Na-p states to the valence band. Additionally, Mg-states slightly contribute to both the valence and conduction bands. These findings confirm the view that the [$MgCl_6$] and [$NaCl_6$] hybridization determines the electronic properties of Na_2MgCl_4. Given the tendency of DFT computations to

Open Access Article. Published on 28 February 2025. Downloaded on 2/21/2026 7:17:04 PM.
This article is licensed under a Creative Commons Attribution-NonCommercial 3.0 Unported Licence.

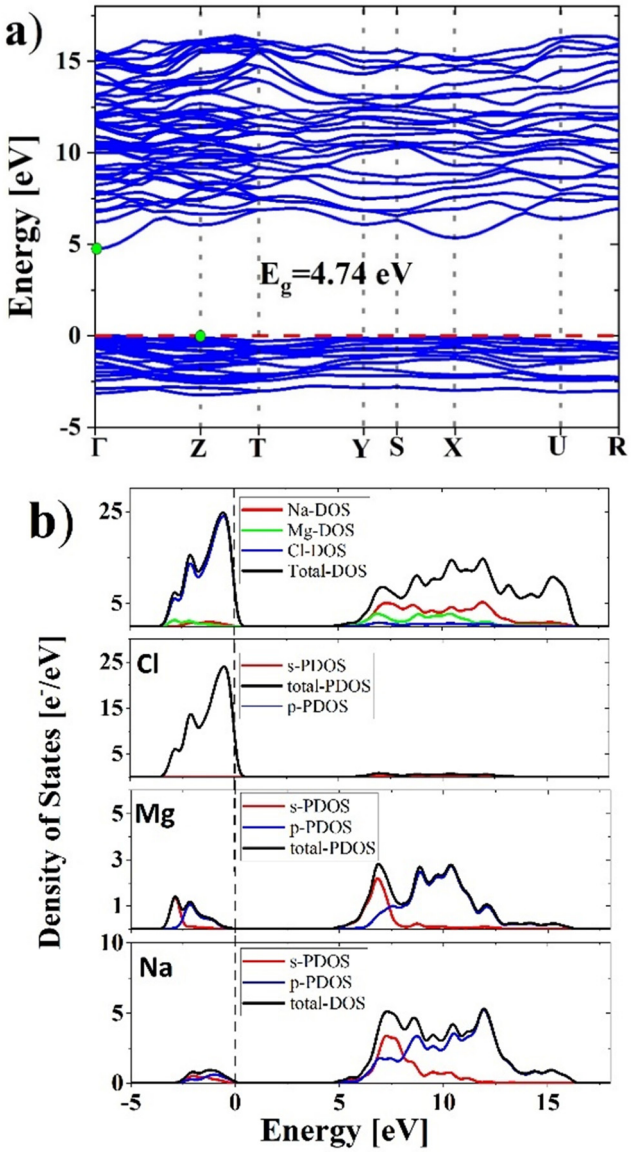

Fig. 2 (a) Band structure and (b) density of states of the Na_2MgCl_4 structure; dashed red and black lines represent the Fermi level. Green bullets in (a) represent the valence band maximum at the Z point and conduction band minimum at the Γ point.

underestimate the band gap and the lack of experimental verification, the predicted energy gap must be considered as a lower bound.[42]

3.2 Mechanical properties and mechanical stability

Another significant challenge in developing solid-state electrolytes is the determination of their mechanical properties and mechanical stability.[43–45] These properties are crucial for understanding the malleability and resistance to mechanical degradation of the solid-state electrolyte, which ensures good contact with the electrodes and minimal volume expansion during the charge/discharge process.[43–45]

The elastic constant matrix (C_{ij}) describes the mechanical response of a crystalline structure. The Born criteria establish

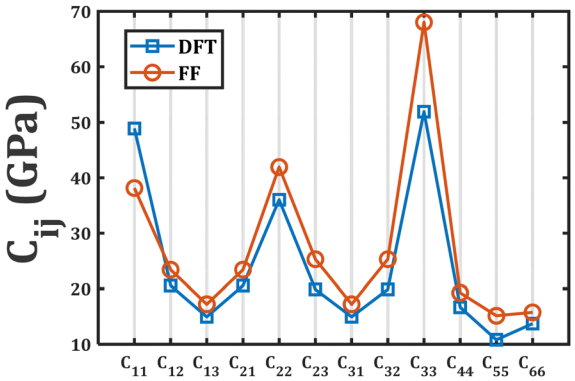

Fig. 3 Elastic constant matrix elements obtained *via* DFT and FF computations.

that the energy for an arbitrary homogeneous deformation loaded by an infinitesimal strain is positive.[46] In this sense, the C_{ij} matrix should be positive definite inferring positive eigenvalues (λ). The C_{ij} matrix elements of Na_2MgCl_4 derived from DFT (C_{ij}^{DFT}) and force field (C_{ij}^{FF}) computations are given in Fig. 3; their values are included in the ESI,† file. Although small differences between C_{ij}^{DFT} and C_{ij}^{FF} are observed, due to the lack of experimental verifications, these values must be considered as lower and upper bounds.

The computed eigenvalues of the elastic constant matrix derived from DFT computations are λ_1^{DFT} = 10.81, λ_2^{DFT} = 13.72, λ_3^{DFT} = 16.75, λ_4^{DFT} = 18.47, λ_5^{DFT} = 35.53 and λ_6^{DFT} = 82.86 GPa, and from the force field method are λ_1^{FF} = 15.13, λ_2^{FF} = 15.75, λ_3^{FF} = 15.93, λ_4^{FF} = 19.26, λ_5^{FF} = 35.92 and λ_6^{FF} = 96.27 GPa. In both approaches, all eigenvalues are positive, confirming that the Na_2MgCl_4 compound is mechanically stable.[46]

The bulk and shear moduli measure the resistance to both deformation and volume change.[47–51] The Voigt approximation assumes a uniform strain on the lattice structure,[49] in which the bulk and shear moduli are given by eqn (4) and (5), respectively:

$$B_{Voigt} = \frac{1}{3}[C_{11} + 2C_{12}] \quad (4)$$

$$G_{Voigt} = \frac{1}{5}[C_{11} - C_{12} + 3C_{44}] \quad (5)$$

The Reuss approximation adopts a uniform stress on the lattice structure,[50] deriving the shear and bulk moduli from the compliance matrix ($S_{ij} = C_{ij}^{-1}$) elements, whereas the Hill approximation combines both the Voigt and Reuss theories (*cf.* eqn (6)–(8)):[51,52]

$$B_{Reuss} = 27[S_{11} + 2S_{12}]^{-1} \quad (6)$$

$$G_{Reuss} = 15[4S_{11} - 3(S_{12} + S_{44})]^{-1} \quad (7)$$

$$B_{Hill} = \frac{1}{2}(B_{Voigt} + B_{Reuss});\ G_{Hill} = \frac{1}{2}(G_{Voigt} + G_{Reuss}) \quad (8)$$

Table 2 collects the results of mechanical properties of the Na_2MgCl_4 structure. The computed bulk, shear (Hill approximation)

 This journal is © the Owner Societies 2025

Open Access Article. Published on 28 February 2025. Downloaded on 2/21/2026 7:17:04 PM.
This article is licensed under a Creative Commons Attribution-NonCommercial 3.0 Unported Licence.

Table 2 Mechanical properties calculated using DFT and force field (FF) methods (B, G and E in GPa)

	Method	Reuss	Voigt	Hill
Bulk modulus (B)	DFT	27.19	27.52	27.35
	FF	29.53	31.11	30.32
Shear modulus (G)	DFT	12.83	13.67	13.25
	FF	13.85	15.51	14.68
B/G	DFT	2.12	2.01	2.06
	FF	2.13	2.01	2.07
M	DFT	1.63	1.65	1.64
	FF	1.53	1.62	1.42

	Direction	x	y	z
Young's modulus (E)	DFT	36.84	23.48	40.61
	FF	24.89	23.96	52.39
Universal anisotropy (A^U)	DFT	0.34		
	FF	0.65		
A_B	DFT	0.01		
	FF	0.03		
A_G	DFT	0.03		
	FF	0.06		
Kleinman coefficient (K)	DFT	0.56		
	FF	0.72		
Cauchy pressure C_{12}–C_{44} (GPa)	DFT	3.92		
	FF	4.16		

and Young moduli (z-direction) amount to 30.22, 14.68 and 52.39 GPa, respectively. The values of mechanical properties are comparable to those of other battery materials.[18,53–55] For instance, the bulk, shear and Young moduli of Na_6MgCl_8 amount to 26.57, 15.00 and 42.86 GPa, respectively.[18,54] In our recent study,[18] these magnitudes computed for the $Na_2Mg_3Cl_8$ structure amount to 34.22, 14.47 and 40.49 GPa for bulk, shear and Young moduli, respectively.[18] Reported values of other Na-antiperovskite materials such as Na_3OCl and Na_3OBr are slightly larger.[55]

The Young modulus is calculated by an approximation such as in eqn (9):

$$E = \frac{9BG}{3B + G} \tag{9}$$

When the bulk modulus is larger than the shear modulus, the compound is more vulnerable to shape deformation than volume change. In addition, a larger Young value with respect to the bulk modulus indicates that the compound is more resistant against uniaxial compression or tension than hydrostatic pressure. As shown in Table 2, these values, computed from DFT and FF methods within the Hill approximation, reveal that the Na_2MgCl_4 structure is more vulnerable to shape deformation and resistant against uniaxial compression than volume change and hydrostatic pressure.

Ductility and brittleness criteria are assessed using Pugh's ratio (B/G),[56] considering the degree of elastic anisotropy, which is crucial for understanding the anisotropy of chemical bonding. Table 2 shows that all B/G values exceed the 1.75 limit, which indicates whether a material is classified as ductile or brittle.[56] Na_2MgCl_4 is found to be a ductile material, with direct implications for manufacturing and volume change during battery cycling. For its part, the Cauchy pressure (C_{12}–C_{44}) defines the failure of a material.[57] While a positive Cauchy pressure indicates ductility, a negative value points out brittleness.[57] The Cauchy pressure values computed by DFT and force field methods are both positive, confirming the ductile nature of the Na_2MgCl_4 compound.

Similar values of Cauchy pressure and B/G have been reported for other SSEs.[57] Appropriate ductile solid-state electrolytes are particularly desirable, accommodating the strains and stresses that arise at the interface between electrodes during the cycling process.[58–61] In summary, the ductility nature of the Na_2MgCl_4 lattice structure ensures its stability and high performance.

The percentage of anisotropy regarding compressibility (A_B) and shear (A_G) for nanocrystalline samples, including the universal anisotropy (A^U), are defined by eqn (10):[53,54,62]

$$A_B = \frac{B_{Voigt} - B_{Reuss}}{B_{Voigt} + B_{Reuss}};\ A_G = \frac{G_{Voigt} - G_{Reuss}}{G_{Voigt} + G_{Reuss}},$$
$$A^U = 5\left(G_{Voigt}/G_{Reuss}\right) + \left(B_{Voigt}/B_{Reuss}\right) - 6 \tag{10}$$

The A_B and A_G values tend to zero, indicating that the Na_2MgCl_4 structure exhibits an elastic isotropy.[62] On the contrary, from the A^U, the material is not extremely anisotropic. Variations of Young's modulus which are observed along crystallographic directions are reflected in the universal anisotropy index.

The Kleinman coefficient (K) has been utilized to study the internal contraction stability of materials, revealing their resistance to both stretching and bending, as well as their ability to withstand external forces while maintaining structural integrity.[63] The K parameter is defined by eqn (11):

$$K = (C_{11} + 8C_{12})/(7C_{11} + 2C_{12}) \tag{11}$$

The K value ranges between $0 \leq K \leq 1$. K-Values closer to one indicate a higher contribution towards bond bending, while values approaching zero imply a greater contribution towards bond stretching.[63] From the results compiled in Table 2, the Na_2MgCl_4 compound is more likely to have bond stretching nature according to DFT computations (K = 0.56) than that by using force field approximation (K = 0.72). The latter shows more of bond bending nature. It is expected that DFT values are more reliable.

To provide more information about a material for industrial and commercial use, one can calculate the machinability index (M).[64,65] Useful details, such as hardness, machine tool durability, operational capacity, and cutting form offer valuable insights into the machinability of materials.[64,65] These factors collectively help to determine the efficiency, precision, and overall effectiveness of machining processes for solid-state electrolytes.[64,65] M is described by the ratio of the bulk modulus (B) to shear resistance (C_{44}): $M = B/C_{44}$.[64,65]

Open Access Article. Published on 28 February 2025. Downloaded on 2/21/2026 7:17:04 PM. This article is licensed under a Creative Commons Attribution-NonCommercial 3.0 Unported Licence.

When the machinability index exceeds a value of 1.45, the compound is considered as suitable for manufacturing.[64,65] The values presented in Table 2 show that the Na_2MgCl_4 is applicable for device fabrication (except for the case of polycrystalline approximation (Hill) derived from force field computations).

In summary, the Na_2MgCl_4 compound is predicted to be mechanically stable, having desirable mechanical properties. Its elasticity properties are not uniform in all directions, but the variation is not very pronounced.

3.3. Intrinsic defect chemistry and dopant incorporation mechanisms in the Na_2MgCl_4 lattice structure

The influence of doping on the electrochemical performance of various Na-based solid-state electrolytes (SSEs) is well-known.[1–3,66–68] This section explores the Na_2MgCl_4 defect chemistry related to intrinsic point defects and the impact of doping with divalent and trivalent ions. The starting point of the defect energetics consists in the exploration of intrinsic defects of Na_2MgCl_4. Three basic Schottky defect mechanisms are considered. The first one considers the full Na_2MgCl_4 Schottky scheme written in the Kröger–Vink notation as described by eqn (12):[69]

$$2Na_{Na}^{\times} + Mg_{Mg}^{\times} + 4Cl_{Cl}^{\times} \rightarrow 2V_{Na}^{'} + V_{Mg}^{''} + 4V_{Cl}^{\bullet} + Na_2MgCl_4 \quad (12)$$

where $Na_{Na}^{\times}$, $Mg_{Mg}^{\times}$ and $Cl_{Cl}^{\times}$ represent the Na^+, Mg^{2+} and Cl^- ions occupying their atomic position in the Na_2MgCl_4 lattice structure, respectively, and $V_{Na}^{'}$, $V_{Mg}^{''}$ and $V_{Cl}^{\bullet}$ denote Na-, Mg- and Cl-vacancies, respectively. The formation of a NaCl Schottky defect is given by eqn (13):

$$Na_{Na}^{\times} + Cl_{Cl}^{\times} \rightarrow V_{Na}^{'} + V_{Cl}^{\bullet} + NaCl \quad (13)$$

leading to the stoichiometric $Na_{2-x}MgCl_{4-x}$ composition, in which for each Na vacancy a Cl vacancy is generated for charge compensation. The formation of $MgCl_2$ Schottky defects is described by eqn (14):

$$Mg_{Mg}^{\times} + 2Cl_{Cl}^{\times} \rightarrow V_{Mg}^{''} + 2V_{Cl}^{\bullet} + MgCl_2 \quad (14)$$

which leads to the stoichiometric $Na_2Mg_{1-x}Cl_{4-2x}$ formula. In this case, for each Mg^{2+}-vacancy two Cl-vacancies are created for charge neutrality. In the present study, Frenkel defect type and other intrinsic defect(s) are not considered because they are energetically unfavorable.[37,53,54]

Divalent and trivalent dopants can be incorporated into the Na_2MgCl_4 lattice structure. The incorporation scheme describing the doping with a divalent dopant (M^{2+}) occupying the Mg^{2+}-site in the Na_2MgCl_4 lattice structure is given in eqn (15):

$$MCl_2 + Mg_{Mg}^{\times} \rightarrow M_{Mg}^{\times} + MgCl_2 \quad (15)$$

In eqn (15) the valence charges of both the dopant M^{2+} and host Mg^{2+} ion are equal to each other, implying that no further defect type is required for charge compensation.

The scheme describing the incorporation of a divalent dopant occupying the Na^+-site leading a Na-vacancy is given by eqn (16):

$$MCl_2 + 2Na_{Na}^{\times} \rightarrow M_{Na}^{\bullet} + V_{Na}^{'} + 2NaCl \quad (16)$$

where for each divalent dopant occupying a Na^+-site ($M_{Na}^{\bullet}$) a Na vacancy is generated for charge compensation, resulting in stoichiometric $Na_{2-x}M_xMgCl_4$.

The next incorporation mechanism deals with the introduction of a trivalent dopant (M^{3+}) occupying an Mg^{2+}-site as in eqn (17):

$$MCl_3 + Mg_{Mg}^{\times} + Na_{Na}^{\times} \rightarrow M_{Mg}^{\bullet} + V_{Na}^{'} + MgCl_2 + NaCl \quad (17)$$

where for each trivalent dopant occupying the Mg^{2+}-site one Na-vacancy is required to maintain the charge neutrality of the defective $Na_{2-x}Mg_{1-x}M_xCl_4$ structure. Secondly, the incorporation of a trivalent dopant (M^{3+}) occupying a Na^+-site is as follows (eqn 18):

$$MCl_3 + 3Na_{Na}^{\times} \rightarrow M_{Na}^{\bullet\bullet} + 2V_{Na}^{'} + 3NaCl \quad (18)$$

In eqn (18), a trivalent dopant occupying a Na^+-site ($M_{Na}^{\bullet\bullet}$) leads to two extra charges, which are compensated by two Na-vacancies, resulting in a $Na_{2-2x}M_xMgCl_4$ structure.

The defect energy (E_s) for the Schottky defect types considered is then obtained as follows (*cf.* eqn (19)–(21)):

$$E_s = \frac{1}{3}\left(2E_{vac}^{Na} + E_{vac}^{Mg} + 4E_{vac}^{Cl} + E_L^{Na_2MgCl_4}\right) \quad (19)$$

$$E_s = \frac{1}{2}\left(E_{vac}^{Na} + E_{vac}^{Cl} + E_L^{NaCl}\right) \quad (20)$$

$$E_s = \frac{1}{2}\left(E_{vac}^{Mg} + 2E_{vac}^{Cl} + E_L^{MgCl_2}\right) \quad (21)$$

and for the dopant incorporation mechanism (eqn (22)–(25)),

$$E_s = E_{subs,Mg}^{M^{2+}} + E_L^{MgCl_2} - E_L^{MCl_2} \quad (22)$$

$$E_s = E_{subs,Na}^{M^{2+}} + E_{vac}^{Na} + 2E_L^{NaCl} - E_L^{MCl_2} \quad (23)$$

$$E_s = E_{subs,Mg}^{M^{3+}} + E_{vac}^{Na} + E_L^{NaCl} + E_L^{MgCl_3} - E_L^{MCl_3} \quad (24)$$

$$E_s = E_{subs,Na}^{M^{3+}} + 2E_{vac}^{Na} + 3E_L^{NaCl} - E_L^{MCl_3} \quad (25)$$

according to eqn (12)–(18), respectively, where E_{vac}^{Na}, E_{vac}^{Mg}, and E_{vac}^{Cl} represent the Na-, Mg- and Cl-vacancy energy, respectively, $E_{subs,Mg}^{M^{2+}}$, $E_{subs,Na}^{M^{2+}}$, $E_{subs,Mg}^{M^{3+}}$ and $E_{subs,Na}^{M^{3+}}$ denote the substitution energy of a $M^{2+/3+}$ at a Mg^{2+}–site and Na^+–site, respectively, and E_L^X represents the lattice energy of the X compound involved.

To evaluate defect energies, firstly, the vacancy formation and lattice energies are calculated. The Mg-, Na- and Cl-vacancies are positioned at the centre of R1. The lattice energies of $MgCl_2$ ($R\bar{3}M$), NaCl ($FM\bar{3}M$) and Na_2MgCl_4 are also computed. Four divalent (Ca^{2+}, Ba^{2+}, Sr^{2+} and Zn^{2+}) and two trivalent dopants (Al^{3+} and Ga^{3+}) are considered for which the lattice energies of their respective metal chlorides are computed.

 This journal is © the Owner Societies 2025

Open Access Article. Published on 28 February 2025. Downloaded on 2/21/2026 7:17:04 PM. This article is licensed under a Creative Commons Attribution-NonCommercial 3.0 Unported Licence.

Table 3 Results of the defect energetics of pristine and doped Na_2MgCl_4

(a) Divalent dopant	IR in Å (CN 6)	MCl_2	$E_L^{MCl_2}$ (eV per f.u.)	$E_{subs,Na}^{M^{2+}}$ (eV per dopant)	$E_{subs,Mg}^{M^{2+}}$ (eV per dopant)	Solution energy (eqn number) (22)	(23)
Zn^{2+}	0.74	$ZnCl_2$	−26.93	−14.29	−0.83	−0.42	1.54
Ca^{2+}	0.99	$CaCl_2$	−21.15	−8.56	5.74	0.37	1.50
Sr^{2+}	1.18	$SrCl_2$	−21.14	−8.24	6.07	0.68	1.80
Ba^{2+}	1.35	$BaCl_2$	−20.16	−6.77	7.59	1.23	2.29

Trivalent dopant	IR in Å (CN 6)	MCl_3	$E_L^{MCl_3}$	$E_{subs,Na}^{M^{2+}}$	$E_{subs,Mg}^{M^{2+}}$	(24)	(25)
Al^{3+}	0.54	$AlCl_3$	−55.85	−37.56	−24.89	1.44	4.19
Ga^{3+}	0.62	$GaCl_3$	−51.61	−33.27	−20.79	1.30	4.24

(b) Basic vacancies			Lattice energies (eV per f.u.)			Schottky (eqn number)		
E_{vac}^{Cl}	E_{vac}^{Na}	E_{vac}^{Mg}	$E_L^{Na_2MgCl_4}$	$E_L^{MgCl_2}$	E_L^{NaCl}	(19)	(20)	(21)
4.94	5.10	21.45	−85.35	−26.52	−8.1	−11.32	0.97	2.40

Table 3 includes other energetic quantities for deriving the solution and binding energies. Table 3a firstly shows the resulting solution energies of divalent dopants. In schemes dealing with M^{2+} occupying an Mg^{2+}-site in the Na_2MgCl_4 lattice structure [*cf.* eqn (15)], charge compensation is not required. This scheme results in a stress/strain defect due to the ionic size difference between the dopant and the host Mg^{2+} (0.72 Å) cation with no defect cluster formation.

It is well known that in a doped structure, the charged point defect(s) commonly leads to an intrinsic association, forming localized defect clusters that can inhibit the transport properties. In particular, formation of the $Ba_{Na}^{\bullet} - V_{Na}^{'}$ dimer tends to affect the conducting properties of the material, because a trapping effect is expected due to the high solution energy (2.29 eV per defect).[35,51,52] Besides, formation of a $Zn_{Na}^{\bullet} - V_{Na}^{'}$ cluster with the lowest solution energy of 1.54 eV per defect should reduce the trapping effect with direct implications for the large-scale transport properties of Na_2MgCl_4. For this reason, Zn^{2+} at the dilute limit is fairly bounded with the Na vacancies, thereby enabling the Na migration.

Table 3a includes the results of E_s of M^{3+} doped Na_2MgCl_4 of the two doping schemes considered [eqn (24) and (25)]. The lowest final solution energy is obtained for Ga^{3+} occupying a Na^+–site related to two Na-vacancies as described in eqn (18). The incorporation mechanism with lower defect association is found for the trivalent dopant occupying a Mg^{2+}-site, leading to a Na– vacancy ($M_{Mg}^{\bullet} - V_{Na}^{'}$ dimer) as described by eqn (17), and, in particular, for the Ga^{3+} dopant (1.30 eV per dopant).

Concerning Schottky defect formations, Table 2b contains the calculated results of formation energy of the intrinsic defect in Na_2MgCl_4. Clearly, the most favorable defect mechanism is the one described by eqn (13) involving the NaCl Schottky defect type (0.97 eV per defect). This double chloride structure has the lowest NaCl Schottky energy as compared to other similar compounds.[18,19,27] Besides, the calculated value for Na_2MgCl_4 is half of those reported for Na_3OCl, suggesting a similar phenomenon concerning both Na and Cl concentrations at ambient temperature.[18,19,27,70] In addition, formation energies for the other two Schottky-defect types are likely unfavorable, which confirms the structural stability of the Na_2MgCl_4 compound. This stability is further validated by the vacancy formation energies, that is, the Na-vacancy is the most favorable, followed by the Cl-vacancy, while the Mg-vacancy is associated with the highest formation energy.

In summary, the most abundant defect type is the NaCl Schottky one with low formation energy. The Zn^{2+} and Ga^{3+} ions occupying a Na^+-site in the Na_2MgCl_4 lattice structure are the best dopants with low solution energies, increasing the Na-vacancy concentration with possible implications for the large-scale transport properties of Na_2MgCl_4.

3.4 Predictions of the Na-transport properties of the Na_2MgCl_4 compound

In this section, transport properties, including diffusion and conduction mechanisms, are examined using the bond valence method. The Na^+ diffusion coefficient and conductivity of the electrode/electrolyte material dictate the sodiation/desodiation rate during charge and discharge cycles.[1–5] Transport properties of a material determine its energy density, high power output, and prolonged cycle life in NIBs, especially for emerging applications such as electric vehicles and grid-scale energy storage.[1–20]

Fig. S1a (in the ESI,† file) shows the energy profile *versus* reaction coordinate describing the energetics of Na^+ migration along accessible sites in the Na_2MgCl_4 structure. From Fig. S1a (ESI†), one can note that the predominant migration pathway is the 1D ribbon with lower activation energies (see Fig. S1b, ESI†), and a 3D migration with higher energy costs (Fig. S1c, ESI†).

Fig. 4a displays the energy isosurface describing the Na^+ migration pathways within the Na_2MgCl_4. Several saddle points (denoted with the letter s) and interstitial (denoted with the letter i) sites are identified. The interstitial mechanism

Open Access Article. Published on 28 February 2025. Downloaded on 2/21/2026 7:17:04 PM.
This article is licensed under a Creative Commons Attribution-NonCommercial 3.0 Unported Licence.

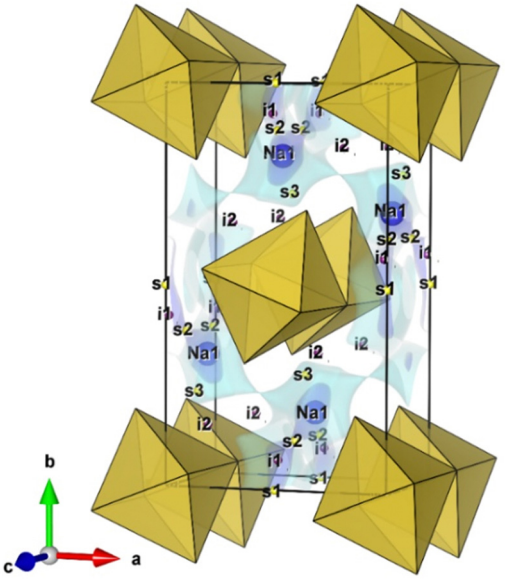

Fig. 4 3D network of Na^+ migration pathways in Na_2MgCl_4 (blue iso-surfaces) calculated using BVSE computations. Yellow polyhedra represent the [$MgCl_6$] octahedra.

described by $Na_{Na}^{\times} \rightarrow V'_{Na} + Na_i^{\bullet}$ appears as the scheme describing the migration mechanism.

The diffusion coefficient and conductivity are computed by using the softBT-GUI code.[41] The conductivity data are derived following the Nernst–Einstein equation in which the diffusion coefficient at each temperature is directly proportional to the conductivity of the mobile ion.[44,71]

Fig. 5 shows the linear Arrhenius-type dependence of diffusion and conductivity in the temperature range of 300–700 K.[72] The activation energy (E_a) for diffusion amounts to 0.20 eV and that for conduction amounts to 0.17 eV. These predicted activation energies indicate that significant increase in mass transport enhances the charge transport process, thereby reducing the conduction activation energy. The Na^+ conductivity and diffusivity at 300 K (σ_{300K} and D_{300K}, respectively) are 0.17 mS cm^{-1} and 1.65 × 10^{-9} cm^2 s^{-1}, respectively.

The E_a value of Na_2MgCl_4, together with the outstanding diffusivity and conductivity at 300 K, meets the requirements for SSEs.[1–15] The activation energy and transport properties at 300 K demonstrate a remarkable compatibility of Na_2MgCl_4 with currently used solid-state electrolytes (SSEs) in Na-ion battery technology.[73–85]

Table 4 provides a detailed comparison of various Na^+-based SSEs, highlighting key properties such as NaCl Schottky energy, room-temperature diffusivity (D_{300K}), conductivity (σ_{300K}), and activation energy (E_a). These parameters are critical for the evaluation of the performance of electrolytes in Na-ion batteries, as they influence ionic transport efficiency and stability.[1–15]

Table 4 includes a range of compounds, namely, Na_6MCl_8 (M = Mg^{2+}, Zn^{2+}, Ca^{2+}, Sr^{2+}, and Ba^{2+}), $Na_2Mg_3Cl_8$ and Na_2MgCl_4. The Na_2MgCl_4 compound exhibits characteristics similar to those of other Na-based SSEs. It has a room-temperature

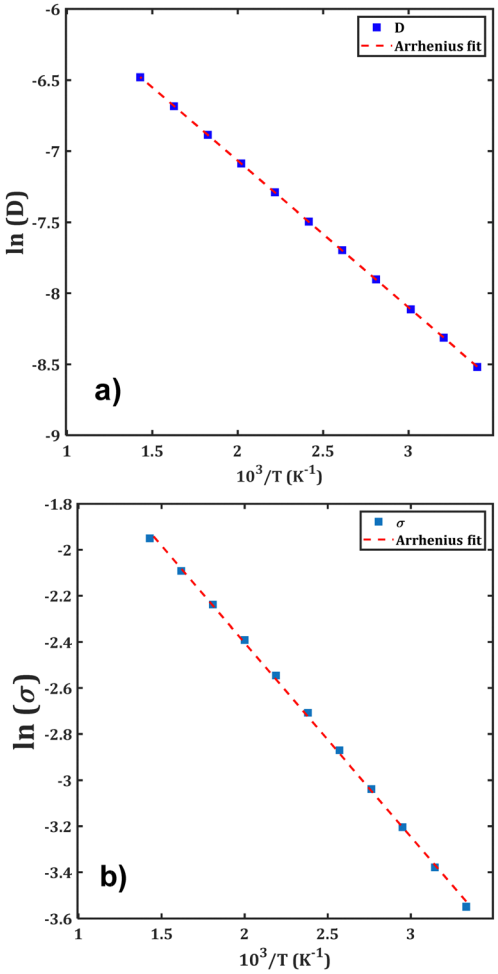

Fig. 5 Linear Arrhenius dependence of the Na^+ ion: (a) diffusion coefficient and (b) conductivity of Na_2MgCl_4.

diffusivity of 1.65 × 10^{-9} cm^2 s^{-1} and a conductivity of 0.17 mS cm^{-1}, positioning it in the mid-range for ionic transport efficiency. Its activation energy is relatively low at 0.17 eV, similar to $Na_2Mg_3Cl_8$, which also has a low activation energy of 0.18 eV.[18] However, Na_2MgCl_4 shows lower conductivity as compared to $Na_2Mg_3Cl_8$, Na_3SbS_4, Na_3PS_4 and $Na_{2.9375}PS_{3.9375}Cl_{0.0625}$ compounds.[18,83–85]

In addition, a recent study on the Na_3YBr_6 solid-state electrolyte, synthesized *via* a solid-state reaction, reveals an experimental activation energy of 0.15 eV, along with a promising electrochemical window, making this Na halide a compelling candidate for all-solid-state sodium batteries.[76] Li_3YCl_6 was reported as a candidate for battery technology having a conductivity of 0.51 mS cm^{-1}.[79,80] Recent advancements in $Na_{1+x}Zr_2Si_xP_{3-x}O_{12}$ superionic conductors have significantly enhanced room-temperature ionic conductivity, reaching an impressive value of 1 mS cm^{-1}.[81,82] Additionally, research on the tetragonal phase of Na_3SbS_4 (293–453 K) showed an activation energy of 0.22 eV and a conductivity of 0.6 mS cm^{-1} at 293 K.[75] As it is shown in Table 4, when comparing the room-temperature conductivity with those of other Li-based SSEs

 This journal is © the Owner Societies 2025

Open Access Article. Published on 28 February 2025. Downloaded on 2/21/2026 7:17:04 PM.
This article is licensed under a Creative Commons Attribution-NonCommercial 3.0 Unported Licence.

Table 4 Comparison of some Na-containing compounds with similar compositions

Compound	NaCl Schottky energy	D_{300K} ($cm^2\ s^{-1}$)	σ_{300K} ($S\ cm^{-1}$)	E_a (eV)
Na_6MgCl_8[54]	1.26	8.33×10^{-12}	2.14×10^{-7}	0.56
Na_6ZnCl_8[54]	1.28	9.12×10^{-12}	1.19×10^{-6}	0.41
Na_6CaCl_8[54]	0.99	1.64×10^{-11}	2.15×10^{-6}	0.39
Na_6SrCl_8[54]	0.97	2.05×10^{-11}	2.69×10^{-6}	0.39
Na_6BaCl_8[54]	0.82	2.46×10^{-11}	3.22×10^{-6}	0.38
$Na_2Mg_3Cl_8$[18]	1.49	3.00×10^{-8}	1.26×10^{-3}	0.18
Na_2MgCl_4	0.97	1.65×10^{-9}	0.17×10^{-3}	0.17
Na_3SbS_4 (cubic)[83]	—	—	1×10^{-3}	0.22
Na_3OCl[37]	1.96	—	—	0.43
Na_3PS_4[84,85]	—	—	0.46×10^{-4}	0.22
$Na_{2.9375}PS_{3.9375}Cl_{0.0625}$[84]	—	—	1.14×10^{-3}	0.25
Li_3YbCl_6[86]	—	—	0.14×10^{-3}	—
$Li_{2.5}Y_{0.5}Zr_{0.5}Cl_6$[87]	—	—	1.4×10^{-3}	—
$Li_{2.556}Yb_{0.492}Zr_{0.492}Cl_6$[88]	—	—	1.58×10^{-3}	—
$Li_{2.7}Yb_{0.7}Hf_{0.3}Cl_6$[89]	—	—	1.1×10^{-3}	—

(orthorhombic structures),[86–89] the Na_2MgCl_4 compound stands in the mid-range for Na^+-ion transport.

Fig. S2 (ESI,† file) illustrates the performance ranking of Na_2MgCl_4 in terms of activation energy and σ_{300K}, as per the dynamic database for solid state electrolyte (DDSE).[90,91] DDSE is a novel and online platform designed for helping solid-state battery research and development.[90,91]

The transport properties of Na_2MgCl_4 are benchmarked against 2532 experimentally studied solid-state electrolytes and 657 computationally explored compounds. The comparison reveals that Na_2MgCl_4, which exhibits a high σ_{300K} (Fig. S2a, ESI†) and a low activation energy of 0.17 eV (Fig. S2b, ESI†), ranks favorably among previously reported SSEs. These results support the promising performance discussed in Table 4 compared with other SSEs.

These favorable transport properties, comparable to those listed in the DDSE (including those collected in Table 4), underscore the potential of Na_2MgCl_4 for synthesis and performance evaluation in sodium-ion battery technology. Overall, the Na_2MgCl_4 double chlorite structure exhibits required transport properties, mechanical stability, and excellent malleability. It thus emerges as a strong SSE candidate for current and future sodium-ion battery technology.

4. Concluding remarks

In this paper, the results of advanced atomistic simulations of the main properties of Na_2MgCl_4 are presented. By combining quantum-based calculations with static and large-scale molecular dynamics simulations, relevant properties related to the key requirements of a material with potential application as a solid-state electrolyte in energy storage applications are disclosed. The results of DFT computations reveal that the Na_2MgCl_4 double chlorite has an isolating characteristic with an energy gap of $\sim$4.7 eV, where the $[MgCl_6]$ and $[NaCl_6]$ hybridization determines its electronic properties. Na_2MgCl_4 is predicted to be mechanically stable and ductile with favorable bulk, shear and Young moduli, ensuring compatibility with possible electrodes and stability.

Defect energetics computations reveal that the most abundant defect type is the NaCl Schottky defect type with low formation energy. The Zn^{2+} and Ga^{3+} occupying a Na^+-site in the Na_2MgCl_4 lattice structure are the best dopants with low solution energies. They increase the Na-vacancy concentration with favorable implications for the large-scale transport properties of Na_2MgCl_4.

The transport properties of Na_2MgCl_4 are evaluated by the bond valence site energy method. Remarkably low Na activation energies for diffusion (0.20 eV) and for conduction (0.17 eV) are predicted. Along with the low activation energies, the Na_2MgCl_4 structure having outstanding diffusivity and conductivity at 300 K (1.65×10^{-9} $cm^2\ s^{-1}$ and 0.17 mS cm^{-1}, respectively) is competitive with contemporary SSEs, underscoring their readiness for high-performance battery applications.

In summary, the double halide Na_2MgCl_4 compound is predicted to be an insulating material with exceptional malleability, where the NaCl Schottky defect plays a key role in its transport properties and is expected to be present in real samples. This compound meets the essential criteria to be considered as an efficient solid-state electrolyte for Na^+-ion batteries. Given the ongoing intensive search for efficient battery materials, we hope that this prediction will inspire subsequent experimental studies.

Author contributions

YAZ: conception, data acquisition and interpretation, original draft preparation, editing, review. JRFG: data acquisition and interpretation, original draft preparation. NAVG: data analysis, editing, review. MPPH: data analysis, editing, review. MTN: conception, project supervision, manuscript editing and review. All authors reviewed the manuscript.

Data availability

The data supporting this article have been included as part of the ESI.†

Conflicts of interest

There are no conflicts to declare.

Acknowledgements

MTN thanks Van Lang University for support. MPPH acknowledges the Ho Chi Minh City University of Technology (HCMUT) and VNU-HCM for supporting this study.

Notes and references

1 G. Assatand and G. M. Tarascon, *Nat. Energy*, 2018, **3**(5), 373–386.

Open Access Article. Published on 28 February 2025. Downloaded on 2/21/2026 7:17:04 PM. This article is licensed under a Creative Commons Attribution-NonCommercial 3.0 Unported Licence.

2 Y. Deng, C. Eames, L. H. B. Nguyen, O. Pecher, K. J. Gri, M. Courty, B. Fleutot, J. Chotard, C. P. Grey, M. S. Islam and C. Masquelier, *Chem. Mater.*, 2018, **30**, 2628–2630.
3 Z. Fu, X. Chen and Q. Zhang, *Wiley Interdiscip. Rev.: Comput. Mol. Sci.*, 2022, e1621.
4 W. Huang, N. Matsui, S. Hori, K. Suzuki, M. Hirayama, M. Yonemura, T. Saito, T. Kamiyama, Y. Sasaki, Y. Yoon, S. Kim and R. Kanno, *J. Am. Chem. Soc.*, 2022, **144**(11), 4989–4994.
5 K. V. Kravchyk, D. T. Karabay and M. V. Kovalenko, *Sci. Rep.*, 2022, **12**(1), 1–10.
6 A. R. Stamminger, B. Ziebarth, M. Mrovec, M. T. Hammerschmidt and R. Drautz, *RSC Adv.*, 2020, **10**(18), 10715–10722.
7 M. Armand and J. M. Tarascon, *Nature*, 2008, **451**(7179), 652–657; D. Larcher and J. M. Tarascon, *Nat. Chem.*, 2015, **7**, 19–29.
8 H. Tian, F. Xin, X. Wang, W. He and W. J. Han, *J. Mater.*, 2015, **1**, 153–169.
9 A. Ahniyaz, I. de Meatza, A. Kvasha, O. Garcia-Calvo, I. Ahmed, M. F. Sgroi, M. Giuliano, M. Dotoli, M. A. Dumitrescu, M. Jahn and N. Zhang, *Adv. Appl. Energy*, 2021, **19**, 100070.
10 B. Zhang, R. Tan, L. Yang, J. Zheng, K. Zhang, S. Mo, Z. Lin and F. Pan, *Energy Storage Mater.*, 2018, 139–159.
11 X. Zhang, D. Wang, X. Qiu, Y. Ma, D. Kong, K. Müllen, X. Li and L. Zhi, *Nat. Commun.*, 2020, **11**, 1–9.
12 Y. S. Su, K. C. Hsiao, P. Sireesha and J. Y. Huang, *Batteries*, 2022, **8**, 1–17.
13 T. H. Wan, F. Ciucci and A. C. S. Appl, *Energy Mater.*, 2021, **4**(8), 7930–7941.
14 L. Fan, S. Wei, S. Li, Q. Li and Y. Lu, *Adv. Energy Mater.*, 2018, **8**, 1702657.
15 M. Hou, F. Liang, K. Chen, Y. Dai and D. Xue, *Nanotechnology*, 2020, **31**(13), 132003.
16 B. Singh, Z. Wang, S. Park, G. Sai Gautam, J. N. Chotard and L. A. Croguennec, *J. Mater. Chem. A*, 2021, **9**, 281–292.
17 K. Chayambuka, G. Mulder, D. L. Danilov and P. H. L. Notten, *Adv. Energy Mater.*, 2018, 1–49.
18 Y. A. Zulueta, J. R. Fernández-Gamboa, T. V. B. Phung, M. P. Pham-Ho and M. T. Nguyen, *RSC Adv.*, 2024, **14**, 33619–33628.
19 A. A. Franco, A. Rucci, D. Brandell, C. Frayret, M. Gaberscek, P. Jankowski and P. Johansson, *Chem. Rev.*, 2019, **119**, 4569–4627.
20 S. Adams, *Solids Solid State Ionics*, 2006, **177**, 1625–1630.
21 S. Adams and R. P. Rao, *Phys. Chem. Chem. Phys.*, 2009, **11**, 3210–3216.
22 Y. A. Zulueta and M. T. Nguyen, *Phys. Chem. Chem. Phys.*, 2023, **25**(41), 27926–27935.
23 I. D. Brown, *Chem. Rev.*, 2009, **109**, 6858–6919.
24 H. Chen, L. L. Wong and S. Adams, *Acta Crystallogr., Sect. B: Struct. Sci., Cryst. Eng. Mater.*, 2019, **75**, 18–33.
25 Y. A. Zulueta and M. T. Nguyen, *Annual Reports in Computational Chemistry*, Elsevier, 2023, vol. 19, pp. 1–43, DOI: **10.1016/bs.arcc.2023.10.004**.
26 B. Tao, D. Zhong, H. Li, G. Wang and H. Chang, *Chem. Sci.*, 2023, **14**(33), 8693–8722.
27 Y. A. Zulueta, M. P. Pham-Ho and M. T. Nguyen, *J. Phys. Chem. Solids*, 2024, **188**, 111916.
28 X. Nie, J. Hu and C. Li, *Interdiscip. Mater.*, 2023, **2**(3), 365–389.
29 H. Dieter Lutz, K. Wussow and P. Kuske, *Z. Naturforsch., B: J. Chem. Sci.*, 1987, **42**, 1379–1386.
30 R. Kanno, Y. Takeda, K. Murata and O. Yamamoto, *Solid State Ionics*, 1990, **39**, 233–244.
31 E. Ulime, A. Pogrebnoi and T. Pogrebnaya, *Br. J. Appl. Sci. Technol.*, 2016, **12**, 1–15.
32 M. C. Payne, M. P. Teter, D. C. Allan, T. A. Arias and J. D. Joannopoulos, *Rev. Mod. Phys.*, 1992, **64**, 1045–1097.
33 D. Vanderbilt, *Phys. Rev. B: Condens. Matter Mater. Phys.*, 1990, **41**, 7892–7895.
34 H. J. Monkhorst and J. D. Pack, *Phys. Rev. B: Condens. Matter Mater. Phys.*, 1976, **13**, 5188–5192.
35 J. D. Gale and A. L. Rohl, *Mol. Simul.*, 2003, **29**, 291–341.
36 Computational Modelling of Zinc Oxide and Related Oxide Ceramics – University of Surrey, **https://openresearch.surrey.ac.uk/esploro/outputs/doctoral/Computational-Modelling-of-Zinc-Oxide-and/99512944702346**, (accessed 30 May 2024).
37 B. A. Goldmann, M. J. Clarke, J. A. Dawson and M. S. Islam, *J. Mater. Chem. A*, 2022, **10**, 2249–2255.
38 B. G. Dick and A. W. Overhauser, *Phys. Rev.*, 1958, **112**, 90–103.
39 N. F. Mott and M. J. Littleton, *Trans. Faraday Soc.*, 1938, **34**, 485–499.
40 J. D. Gale, *J. Chem. Soc., Faraday Trans.*, 1997, **93**, 629–637.
41 L. L. Wong, K. C. Phuah, R. Dai, H. Chen, W. S. Chew and S. Adams, *Chem. Mater.*, 2021, **33**, 625–641.
42 M. G. Medvedev, I. S. Bushmarinov, J. Sun, J. P. Perdew and K. A. Lyssenko, *Science*, 2017, **355**, 49–52.
43 X. Ke, Y. Wang, G. Ren and C. Yuan, *Energy Storage Mater.*, 2020, **26**, 313–324.
44 M. Hou, F. Liang, K. Chen, Y. Dai and D. Xue, *Nanotechnology*, 2020, **31**, 132003.
45 Z. Ding, J. Li, J. Li and C. An, *J. Electrochem. Soc.*, 2020, **167**, 070541.
46 M. Born, K. Huang and M. Lax, *Am. J. Phys.*, 1955, **23**, 474.
47 I. N. Frantsevich, F. F. Voronov and S. A. Bokuta, *Elastic Constants and Elastic Moduli of Metals and Insulators Handbook*, Naukova Dumka, Kiev, 1983, pp. 60–180.
48 F. I. Fedorov, *Theory of Elastic Waves in Crystals*, Springer US, Boston, MA, 1968.
49 W. Voigt, *Lehrbuch der Kristallphysik (BG Teubner Leipzig und 791 Berlin) 980 S; Reproduced 1966 Spring Fachmedien Wiesbaden GmbH*, 1928.
50 A. Reuss, *J. Appl. Math. Mech.*, 1929, **9**, 49–58.
51 R. Hill, *J. Mech. Phys. Solids.*, 1963, **11**, 357–372.
52 R. Hill, *Proc. - R. Soc. Edinburgh, Sect. A*, 1952, **65**, 349–354.
53 Y. A. Zulueta, M. P. Pham-Ho and M. T. Nguyen, *J. Phys. Chem. Solids*, 2024, **188**, 111916.

 This journal is © the Owner Societies 2025

Open Access Article. Published on 28 February 2025. Downloaded on 2/21/2026 7:17:04 PM. This article is licensed under a Creative Commons Attribution-NonCommercial 3.0 Unported Licence.

54 Y. A. Zulueta, M. P. Pham-Ho and M. T. Nguyen, *RSC Adv.*, 2024, **14**, 21644–21652.
55 M. A. Sattar, M. Javed, M. Benkraouda and N. Amrane, *Int. J. Energy Res.*, 2021, **45**, 4793–4810.
56 S. F. Pugh, *London, Edinburgh Dublin Philos. Mag. J. Sci.*, 1954, **45**, 823–843.
57 S. Uddin, A. Das, M. A. Rayhan, S. Ahmad, R. M. Khokan, M. Rasheduzzaman, R. Das, A. Ullah, Y. Arafat and M. Z. Hasan, *J. Comput. Electron.*, 2024, **23**, 1217–1237.
58 J. Smith, A. Johnson and L. Brown, *Batteries*, 2024, **7**, 18.
59 M. Davis, K. Lee and P. Wilson, *Chem. Soc. Rev.*, 2024, **53**, 214.
60 D. Patel, E. Garcia and H. Chen, *Mater. Horiz.*, 2020, **7**, 1701.
61 F. Thompson, G. Wang and J. Zhang, *Energy Mater.*, 2020, **5**, 92.
62 S. I. Ranganathan and M. Ostoja-Starzewski, *Phys. Rev. Lett.*, 2008, **101**, 055504.
63 L. Kleinman, *Phys. Rev.*, 1962, **128**, 2614–2621.
64 R. Ahmed, M. Mahamudujjaman, M. A. Afzal, M. S. Islam, R. S. Islam and S. H. Naqib, *J. Mater. Res. Technol.*, 2023, **24**, 4808–4832.
65 M. Islam, *Chem. Phys. Impact*, 2023, **7**, 100310.
66 Q. Zhao, S. Stalin, C. Z. Zhao and L. A. Archer, *Nat. Rev. Mater.*, 2020, **5**, 229–252.
67 T. H. Wan and F. Ciucci, *ACS Appl. Energy Mater.*, 2021, **4**, 7930–7941.
68 M. Illbeigi, A. Fazlali, M. Kazazi and A. H. Mohammadi, *Solid State Ionics*, 2016, **289**, 180–187.
69 F. A. Kröger, *The Chemistry of Imperfect Crystals*, North-Holland Pub. Co., 1964.
70 H. J. Lee, B. Darminto, S. Narayanan, M. Diaz-Lopez, A. W. Xiao, Y. Chart, J. H. Lee, J. A. Dawson and M. Pasta, *J. Mater. Chem. A*, 2022, **10**, 11574–11586.
71 J. A. Dawson, T. Famprikis and K. E. Johnston, *J. Mater. Chem. A*, 2021, **9**, 18746–18772.
72 L. V. Duong, M. T. Nguyen and Y. A. Zulueta, *RSC Adv.*, 2022, **12**, 20029–20036.
73 N. Wang, K. Yang, L. Zhang, X. Yan, L. Wang and B. Xu, *J. Mater. Sci.*, 2018, **53**, 1987–1994.
74 Q. Zhang, C. Zhang, Z. D. Hood, M. Chi, C. Liang, N. H. Jalarvo, M. Yu and H. Wang, *Chem. Mater.*, 2020, **32**, 2264–2271.
75 R. Jalem, A. Hayashi, F. Tsuji, A. Sakuda and Y. Tateyama, *Chem. Mater.*, 2020, **2020**, 58.
76 X. Y. Niu, X. Y. Dou, C. Y. Fu, Y. C. Xu and X. Y. Feng, *RSC Adv.*, 2024, **14**, 14716–14721.
77 J. A. Dawson, T. S. Attari, H. Chen, S. P. Emge, K. E. Johnston and M. S. Islam, *Energy Environ. Sci.*, 2018, **11**, 2993–3002.
78 L. Wang, Z. Song, X. Lou, Y. Chen, T. Wang, Z. Wang, H. Chen, W. Yin, M. Avdeev, W. H. Kan, B. Hu and W. Luo, *Small*, 2024, 2400195.
79 J. Liang, E. Maas, J. Luo, X. Li, N. Chen, K. R. Adair, W. Li, J. Li, Y. Hu, J. Liu, L. Zhang, S. Zhao, S. Lu, J. Wang, H. Huang, W. Zhao, S. Parnell, R. I. Smith, S. Ganapathy, M. Wagemaker and X. Sun, *Adv. Energy Mater.*, 2022, **12**, 2103921.
80 B. Tao, D. Zhong, H. Li, G. Wang and H. Chang, *Chem. Sci.*, 2023, **14**, 8693–8722.
81 Z. Gao, J. Yang, G. Li, T. Ferber, J. Feng, Y. Li, H. Fu, W. Jaegermann, C. W. Monroe and Y. Huang, *Adv. Energy Mater.*, 2022, **12**, 2103607.
82 E. J. Cheng, T. Yang, Y. Liu, L. Chai, R. Garcia-Mendez, E. Kazyak, Z. Fu, G. Luo, F. Chen, R. Inada, V. Badilita, H. Duan, Z. Wang, J. Qin, H. Li, S. Orimo and H. Kato, *Mater. Today Energy*, 2024, **44**, 101644.
83 H. Wang, Y. Chen, Z. D. Hood, G. Sahu, A. S. Pandian, J. K. Keum, K. An and C. Liang, *Angew. Chem., Int. Ed.*, 2016, **55**, 8551–8555.
84 A. Hayashi, K. Noi, N. Tanibata, M. Nagao and M. Tatsumisago, *J. Power Sources*, 2014, **258**, 420–423.
85 I. H. Chu, C. S. Kompella, H. Nguyen, Z. Zhu, S. Hy, Z. Deng, Y. S. Meng and S. P. Ong, *Sci. Rep.*, 2016, **6**, 33733.
86 J. Park, D. Han, H. Kwak, Y. Han, Y. J. Choi, K.-W. Nam and Y. S. Jung, *Chem. Eng. J.*, 2021, **425**, 130630.
87 K.-H. Park, K. Kaup, A. Assoud, Q. Zhang, X. Wu and L. F. Nazar, *ACS Energy Lett.*, 2020, **5**, 533–539.
88 G. Xu, L. Luo, J. Liang, S. Zhao, R. Yang, C. Wang, T. Yu, L. Wang, W. Xiao, J. Wang, J. Yu and X. Sun, *Nano Energy*, 2022, **92**, 106674.
89 S. Y. Kim, K. Kaup, K.-H. Park, A. Assoud, L. Zhou, J. Liu, X. Wu and L. F. Nazar, *ACS Mater. Lett.*, 2021, **3**, 930–938.
90 F. Yang, E. Campos dos Santos, X. Jia, R. Sato, K. Kisu, Y. Hashimoto, S. Ichi Orimo and H. Li, *Nano Mater. Sci.*, 2024, **6**, 256–262.
91 F. Yang, Q. Wang, E. J. Cheng, D. Zhang and H. Li, *Comput. Mater. Contin.*, 2024, **81**, 3413–3419.